Relationship of Ultrasonic Spectral Parameters to Features of Tissue Microstructure

FREDERIC L. LIZZI, MEMBER, IEEE, MICHAEL OSTROMOGILSKY, ERNEST J. FELEPPA, MEMBER, IEEE, MARY C. RORKE, AND MYKOLA M. YAREMKO, MEMBER, IEEE

Abstract—**Analytical studies have been conducted to investigate the importance of specific tissue features in determining ultrasonic spectral "signatures" that have proven to be diagnostically useful. Three models of tissue microstructure were considered, and calibrated power spectra were computed for a series of scatterer sizes, concentrations, and acoustic impedances. General results were obtained, then specific parameters were employed to simulate studies of the eye and liver. These results were compared to clinical data-base information, and excellent correspondence was found. Studies using acoustic microscopy, test objects, and clinical data are continuing to refine the analytical model.**

I. Introduction

ULTRASONIC tissue characterization techniques are often based on the premise that disease processes alter physical characteristics of tissue and that these alterations can cause observable changes in acoustic scattering properties. Many investigations select an appropriate observation or analysis technique and catalog scattering characteristics from normal and diseased tissues in an effort to identify perturbations that can be correlated with the presence of specific diseases. When such perturbations are identified, the investigations can proceed to fundamental studies of the physical changes in tissue that are responsible for producing them. For example, various investigators have examined the liver [1]–[3], heart [4], and spleen [5] using this approach.

Our investigations have also followed this rationale for ocular examinations (in collaboration with D. J. Coleman, M.D., of Cornell University Medical College) and abdominal examinations (in collaboration with D. King, M.D., of the College of Physicians and Surgeons, Columbia University). Our ocular data base now comprises over 1000 clinical examinations, and we have identified tissue characterization parameters that are correlated with specific diseases (e.g., ocular tumors) [6], [7] and with internal morphological changes induced by therapeutic modalities (e.g., radiotherapy and hyperthermia) [8]. Our liver data base is smaller but growing rapidly with a newly implemented PDP 11/23 acquisition and analysis system. Here we have identified parameters that are promising for examining both diffuse and focal diseases [9].

In studying how the useful observable features that we have identified are related to tissue microstructure, we have employed optical microscopy, analytical modeling and, more recently, acoustic microscopy. All three of these approaches are important in identifying those morphological features that are sensed by our measurement techniques.

This report discusses some of the analytical approaches we are employing to determine the relative importance of various tissue features in producing tissue "signatures." These approaches treat simple conceptual models of tissue microstructure and relate our basic measurement parameters to three properties of tissue. Specifically, these are the effective sizes, concentrations, and acoustic impedances of tissue elements. The model has given us insight into how each of these properties influences our ultrasonic measurements. In ophthalmology we have compared analytical results to our clinical ocular-tumor data base [10] and found that the most important tissue feature sensed with our techniques is the effective size of scatterers; we are now using these results to estimate mean effective scatterer size and to estimate a new parameter that combines scatterer concentration and acoustic impedance. In liver studies we have used the model to determine how local perturbations in these tissue features would affect ultrasonic spectra. For example, we are examining the possibility that "patchy" tissue changes, associated with certain disease processes, might be responsible for producing spatial variations that we have observed in spectral measurements of the liver.

The analytical model has proven very helpful in these evaluations and has delineated specific features and dimensions for careful study with optical microscopy. Perhaps more importantly, the model is directly related to acoustic microscopy, and digitally processed acoustic micrograms are now providing key information for more advanced studies within our analytical framework.

This paper briefly summarizes our clinical processing techniques, describes our analytical model of tissue scattering, and then presents computed results relevant to ocular and liver examinations. The ocular results are compared to our data-base observations, while the liver results are discussed in terms of possible spectral perturbations

Manuscript received June 12, 1986; revised August 11, 1986. This work was supported in part by NIH Grants EY-01212, EY-01813, and CA-38400.

The authors are with the Riverside Research Institute, 330 West 42nd Street, New York City, NY 10036.

IEEE Log Number 8612686.

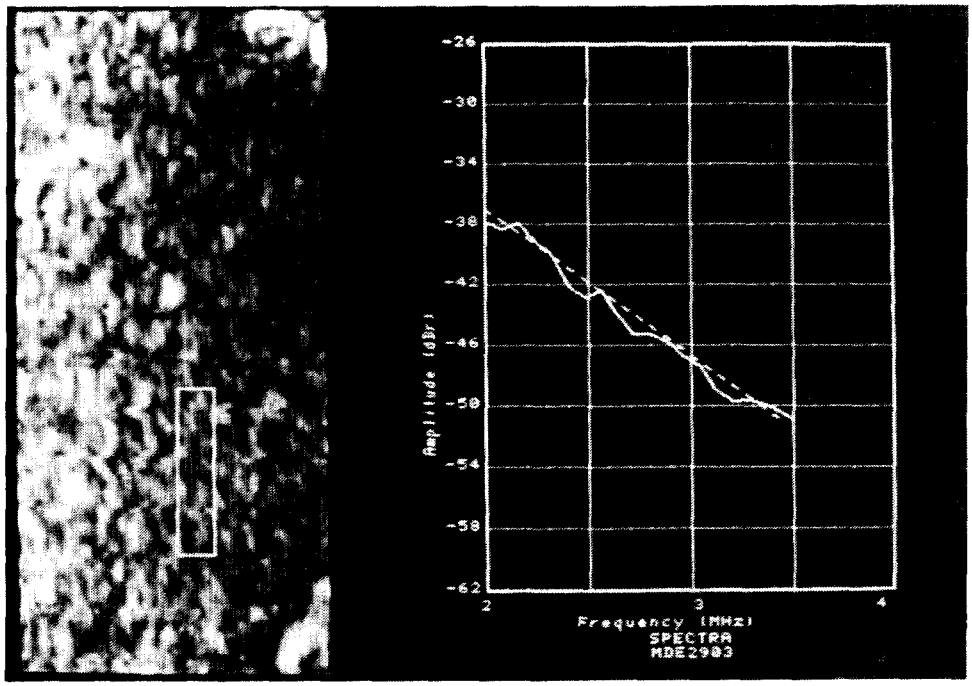

Fig. 1. Computer-generated display showing B-mode image of liver, superimposed analysis region, and calibrated power spectrum.

that may be induced by local variations in scatterer properties.

II. Ultrasonic Spectrum Analysis Techniques

The methods we employ for tissue characterization are based upon calibrated spectrum analysis. These techniques and our digital acquisition and processing system have been described previously [6], [11], [12], and they are very briefly summarized here to provide a background for subsequent discussions. The digital systems we have implemented are interfaced with a number of conventional ultrasonic real-time and immersion scanners; they digitize samples of RF echo signals, as measured at the transducer, and transfer acquired samples to a computer for analysis and display. A number of systems have been implemented using DEC PDP-11 series computers with UNIBUS and, more recently, Q-BUS architectures. Data are acquired from a range segment near the transducer's focal point over a sequence of 100–128 adjacent scan lines; typically, 1 Kbyte of data is acquired per scan line. An entire scan comprising 128 Kbytes is acquired in as little as 30 ms. Sampling rates are set to exceed the Nyquist rate and depend upon the center frequency employed (typically, 10 MHz for ocular examinations and 3 MHz for abdominal examinations).

The acquired RF data are used to compute a B-mode image which is displayed by an integrated digital imaging system; Fig. 1 shows a typical liver image covering an area 4 cm in depth (or range) and 12 cm in cross range. The physician can use these images to demarcate a region for analysis with a variety of processing techniques. The basic analysis technique involves calibrated power spectrum analysis. For each scan-line segment within the selected region, a Hamming weighting function is applied to the corresponding stored RF data, and a Fourier transform is computed. The squared magnitudes of the resultant spectra from each scan line are then averaged and divided by a calibration spectrum (derived from the front surface of a flat plate) to remove various frequency-dependent transfer functions associated with electronic units and the transducer [12]. This calibrated power spectrum is then displayed (in dB) over the frequency range that has been found to produce adequate signal-to-noise levels. (This range is typically 5–15 MHz for ocular examinations and 2–3.5 MHz for liver examinations.)

As shown in Fig. 1, such spectra (expressed in dB) usually exhibit quasi-linear shapes, and we have incorporated linear regression analysis to determine the intercept (extrapolated spectral value of 0 MHz) and slope (with respect to frequency) of the best linear fit [13]. (Other useful descriptive parameters have also been evaluated, but are not addressed in this paper.) These regression parameters are very useful in tissue analysis, but they must be interpreted from different perspectives depending on the examined organ. For ophthalmology, if the ocular lens is avoided, attenuation and refraction are minimal in all media interposed between the transducer and the examined structure; thus the absolute values of the intercept and slope values may be interpreted directly. In liver examinations the interposed tissue segments introduce significant frequency-dependent attenuation which affects slope values; intercept values may be not affected if attenuation varies linearly with frequency (i.e., if it can be expressed in units of dB/MHz · cm). Thus, to characterize abdominal tissues, we use the intercept value and several relative measures of spatial variations of slope that are not influ-

enced by intervening tissue. Specifically, the progressive decrease in slope as a function of range is used to estimate attenuation, and local departures from this progression are used as an index of structural heterogeneity [9].

The following sections examine how these spectral regression parameters are related to scatterer properties. In the eye, spectral slope will be shown to depend upon scatterer size while spectral intercept will be shown to depend upon the sizes, concentrations, and relative acoustic impedances of scattering elements. Because the values of ocular parameters can be considered in an absolute sense, the analytic results can be compared directly to the ocular-tumor data base. In the liver, spectral intercept is related to the three tissue properties already mentioned, and spectral slope variations can be interpreted in terms of local variations in scatterer size.

III. Analytical Framework

The analytical results to be discussed are derived from the general equations presented in a previous report [12]. That report treats the case of weakly scattering tissues examined in the focal zones of transducers typically used in diagnostic ultrasound. Based on these conditions and the assumption that tissue microstructure can be described in terms of wide-sense stationary statistics, the report showed that the averaged calibrated power spectrum is an estimate of the ensemble spectrum $\hat{S}$ as follows:

$$\hat{S} = 4k^2 \int_{-\infty}^{\infty}\int_{-\infty}^{\infty}\int_{-\infty}^{\infty} R_\zeta(\Delta \boldsymbol{x})\, R_D(\Delta y, \Delta z) \cdot R_G(\Delta x)\, e^{j2k\Delta x}\, d\Delta y\, d\Delta z\, d\Delta x \tag{1}$$

where $k = 2\pi f/c$ is the wavenumber, f is the temporal frequency, and c is the speed of acoustic propagation. $R_\zeta(\boldsymbol{\Delta x})$ denotes the spatial autocorrelation function of Z/Z_0, where Z is the acoustic impedance of the scatterers and Z_0 is the mean acoustic impedance of the entire examined tissue; $\boldsymbol{\Delta x}$ refers to the set of three-dimensional lagged coordinates Δx, Δy, and Δz where Δx is specified along the propagation direction. $R_D(\Delta y, \Delta z)$ and $R_G(\Delta x)$ have the form of autocorrelation functions descriptive of the beam's two-way directivity function $F^2(y, z)$ and of the gating function $g(x)$, respectively. These functions are expressed explicitly in terms of the range (x) and cross range (y, z) coordinates as

$$R_D(\Delta y, \Delta z) = \left(\frac{k^2a^2}{4\pi R^2}\right)^2 \int_{-\infty}^{\infty}\int_{-\infty}^{\infty} F^2(y, z)\, F^2(y + \Delta y, z + \Delta z)\, dy\, dz \tag{2}$$

$$F(y, z) = 2J_1(ka(y^2 + z^2)^{1/2}/R)/(ka(y^2 + z^2)^{1/2}/R) \tag{3}$$

$$R_G(\Delta x) = \int_{-\infty}^{\infty} g(x)\, g(x + \Delta x)\, dx \tag{4}$$

where a is the radius of the transducer aperture and R is the range between the transducer and center of the analyzed tissue segment. The function $F^2(y, z)$ describes the beam directivity function in the focal zone, and (3) states its theoretical expression in the focal zone of a typical transducer where J_1 represents a Bessel function of the first kind and first order.

The preceding results were derived for cases where the focused beam is sufficiently narrow to permit the curved focused wavefront to be approximated as a segment of a plane wave. This condition is usually satisfied in ophthalmology [12]. When this is not the case, the expressions are still valid when expressed in spherical coordinates, whose origin is the center of the transducer aperture. (In such cases, near the focus the wavefront can be approximated as a segment of a sphere, and a suitable calibration target may consist of a curved surface whose radius of curvature is equal to R.)

The result for $\hat{S}$ thus depends upon three primary factors: R_ζ, which is tissue-dependent; R_D, which is transducer-dependent; and R_G, which is selected during processing. Before proceeding to examine results for specific realizations of R_ζ, we will consider typical values of R_D and R_G and examine when these functions are significant in clinical examinations. Of particular interest are situations where these functions may be considered to be constants.

First, consider the function R_G defined by (4), and note that the weighting function $g(x)$ determines the length of the analyzed range segment shown in Fig. 1. Usually, $g(x)$ is chosen to be a slowly varying Hamming function whose length L is sufficiently large for adequate spectral resolution but not large enough to introduce signficant frequency-dependent attenuation within the analyzed range segment. Specifically, for an analysis segment centered at x_0,

$$g(x) = \begin{cases} 0.08 + 0.92\cos^2\left(\pi(x - x_0)/L\right), & |x - x_0| \le L/2 \\ 0, & |x - x_0| > L/2. \end{cases} \tag{5}$$

For ophthalmology, L is typically chosen to be 2 mm; for abdominal studies a value of 5 mm is often used.

Given the foregoing expression for $g(x)$, R_G is evaluated from (4) as

$$R_G(\Delta x) = \begin{cases} \left[0.78\,\frac{L}{4\pi}\sin\left(2\pi|\Delta x|/L\right)\right] + \left[(L - |\Delta x|)\left(0.29 + 0.11\cos\left(2\pi|\Delta x|/L\right)\right)\right], & |\Delta x| \le L \\ 0, & |\Delta x| > L. \end{cases} \tag{6}$$

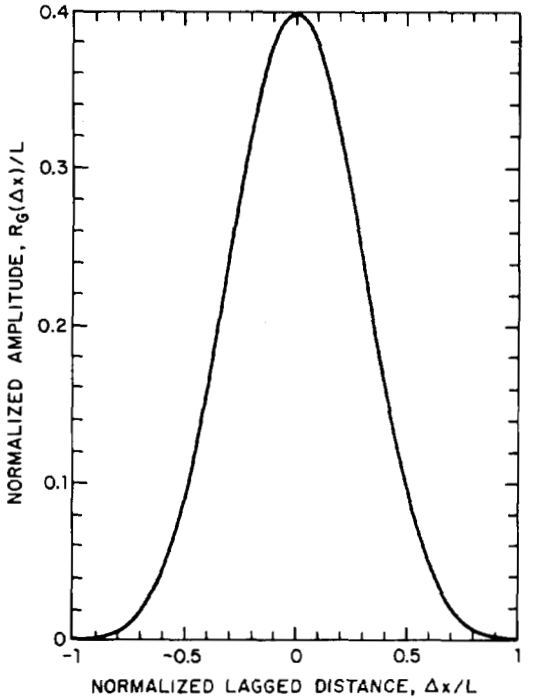

Fig. 2. Plot of $R_G(\Delta x)$.

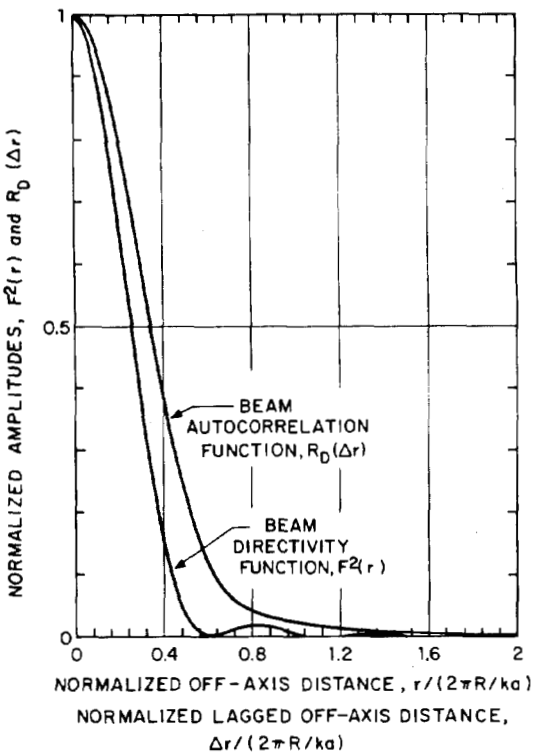

Fig. 3. Plots of beam directivity function $F^2(r)$ versus normalized off-axis distance r, and autocorrelation function $R_D(\Delta r)$ versus normalized off-axis lagged distance. Amplitude of R_D is divided by $0.361\ k^2a^2/4\pi R^2$. Both r and Δr are divided by $2\pi R/ka$.

This function is plotted in Fig. 2. Note that for $|\Delta x|$ smaller than about $0.15L$ the function is relatively constant at $0.4L$ (to within ten percent); this value of Δx corresponds to 0.3 mm for the eye and 0.8 mm for the liver, respectively.

Next, consider the function R_D as defined by (2) and (3). This function has been evaluated numerically and is plotted in Fig. 3. Here, Δr is used to represent the lagged off-axis distance $(\Delta y^2 + \Delta z^2)^{1/2}$, and r is used to represent $(y^2 + z^2)^{1/2}$. The result is a smoothly varying function that can be approximated to a very close degree by a Gaussian curve. The figure shows that R_D is relatively constant at a value of $0.361\ k^2a^2/(4\pi R^2)$ (to within ten percent) for values of the normalized distance variable that are less than about 0.15. For typical ocular examinations (a = 5 mm, R = 35 mm) this corresponds to a lagged off-axis distance of 0.1 mm at the highest frequency of interest (15 MHz). For typical liver examinations (a = 5 mm, R = 60 mm) it corresponds to a value of 0.8 mm at the highest frequency of interest (3.5 MHz).

In summary, the results shown in Figs. 2 and 3 indicate that R_G and R_D may be reasonably approximated as constants over ranges of $|\Delta x|$ and $|\Delta r|$ that are smaller than 0.3 mm and 0.1 mm, respectively, for ocular examinations. For abdominal examinations these approximations are reasonable for $|\Delta x|$ and $|\Delta r|$ smaller than 0.8 mm. These results will be employed in the next section.

IV. Specific Scattering Cases

The results presented in the preceding section will be used to examine specific cases of scattering that are relevant to clinical situations. This involves selecting appropriate forms of R_ζ and using values of frequencies, ranges, and transducer dimensions appropriate to the type of examination being conducted. Then $\hat{S}$ and its linear regression parameters will be computed. First, scattering models that relate to ocular structures will be examined, and theoretical spectral parameters (slope and intercept) will be compared to the clinical tumor data base. Then models relating to the liver will be examined.

A. Ocular Scattering

In analyzing scattering from ocular structures, a suitable function must be chosen for R_ζ. This spatial autocorrelation function of relative acoustic impedance may be determined from an analysis of thin-section acoustic micrograms as we are currently investigating. For this paper we consider three simple tissue models whose autocorrelation functions seem relevant to ocular tissue microstructure. The first model considers tissue to comprise a diffuse spatial distribution of identical spherical particles with uniformly random positions and relatively low concentration. In this case the autocorrelation function is primarily determined by the three-dimensional autocorrelation function of a single sphere. This situation is relevant to homogeneous tumors (e.g., certain melanomas) that contain lipid- and melanin-filled histiocytes whose acoustic impedances are expected to differ from those of surrounding cells; the diameters of these particles are on the order of tens of micrometers. In addition, this model would apply to the small lipid-filled vacuoles seen in some experimental tumors following hyperthermia treatments. These

spherical particles are sometimes seen to form aggregates that, to a first degree of approximation, may be simply treated as larger effective spherical particles. Aggregates may also be considered in terms of the other autocorrelation functions to be described. The other tissue models for consideration are similar to those treated in a somewhat different context by Nicholas [2]; these exhibit Gaussian and exponential autocorrelation functions.

The autocorrelation functions for each of these models are written as R_1, R_2, and R_3, referring to the spherical distribution model, the Gaussian model, and the exponential model, respectively:

$$R_1(\Delta x) = K\left[1 - \frac{3}{4}\frac{|\Delta x|}{\rho} + \frac{1}{16}\frac{|\Delta x|^3}{\rho}\right], \quad |\Delta x| \le 2\rho$$
$$= 0, \quad |\Delta x| > 2\rho \tag{7a}$$

$$R_2(\Delta x) = Ke^{-(1.17|\Delta x|/\rho)^2} \tag{7b}$$

$$R_3(\Delta x) = Ke^{-1.04|\Delta x|/\rho} \tag{7c}$$

where ρ is the effective scatterer radius and

$$K = \frac{4}{3}\pi\rho^3 CQ^2. \tag{8}$$

Here C denotes scatterer concentration (number of scatterers/unit volume) and Q represents the fractional difference of acoustic impedance between the scatterers and the medium. For purposes of comparison, the effective scatterer radius is defined as the value of $|\Delta x|$ at which all of the autocorrelation functions have an equal correlation volume. (Note that in the aforementioned autocorrelation functions we have neglected a constant term equal to the square of the mean of $(Z - Z_0)/Z_0$; this term would introduce a coherent spectrum previously shown to be negligible over the analysis frequency band [12].)

The autocorrelation functions of (7) are plotted in Fig. 4. For the current analysis we will treat cases for which scatterer diameters are 0.1 mm or less and, therefore, we will assume that R_D and R_G are constant as discussed earlier. This range of diameters will be shown to be very significant for interpreting much of our clinical data for ocular tumors.

The power spectra $\hat{S}$ corresponding to each of three autocorrelation functions are calculated by substitution into (1) employing the approximations

$$R_D(\Delta y, \Delta z) \approx R_D(0) = 0.361\, k^2a^2/4\pi R^2$$
$$R_G(\Delta x) \approx R_G(0) = 0.4\, L. \tag{9}$$

Denoting computed spectra by $\hat{S}_i$, where the subscript i corresponds to the subscript of R_i in (7), yields

$$\hat{S}_1(k) = 12\pi\,\rho K\, R_D(0)\, R_G(0)\left[j_1(2k\rho)\right]^2 \tag{10a}$$

$$\hat{S}_2(k) = 4\pi^{3/2}k^2(\rho/1.17)^3\, KR_D(0)\, R_G(0)e^{-(k\rho/1.17)^2} \tag{10b}$$

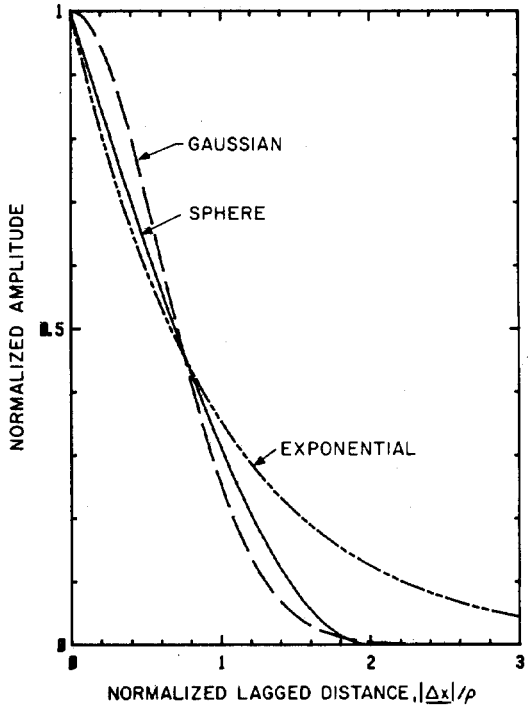

Fig. 4. Plots of three autocorrelation functions R_i.

$$\hat{S}_3(k) = 32\pi k^2(\rho/1.04)\, KR_D(0)\, R_G(0)\left[(\rho/1.04)^2 + 4k^2\right]^{-2} \tag{10c}$$

where $j_1(2k\rho)$ is a spherical Bessel function of the first kind and first order.

To compare these results with clinical ocular data, we substitute typical values of a and R (5 mm and 35 mm, respectively), select $CQ^2 = 1$, and convert to decibels. Results for each of the foregoing spectral functions are shown for various scatterer diameters in Fig. 5. Note that for other values of CQ^2 the amplitude of these plots is increased by 10 log CQ^2, but the shape of the curves, expressed in dB, is not altered as may be seen by converting (10) to decibel units and employing (8).

Fig. 5 shows that when the scatterer diameter is less than about 0.01 mm, all the analyzed autocorrelation functions result in spectral slopes that are approximately proportional to the fourth power of frequency, as expected for Rayleigh scattering. As the diameter becomes larger, the spectra vary less rapidly with increasing frequency and the spectra tend to "flatten." At still larger values of diameter the different forms of the autocorrelation function produce different spectral features. For these large diameters the spherical model produces scalloped spectra (due to resonance phenomena associated with the finite spherical dimensions), the Gaussian autocorrelation function produces negatively sloped spectra, and the exponential function produces flat spectra. The spectral scalloping obtained for the sphere model occurs because we have assumed that only one value of diameter exists; in practical cases a range of sphere sizes would be present, and the sharply defined resonances expected for large scatterers may not be observed.

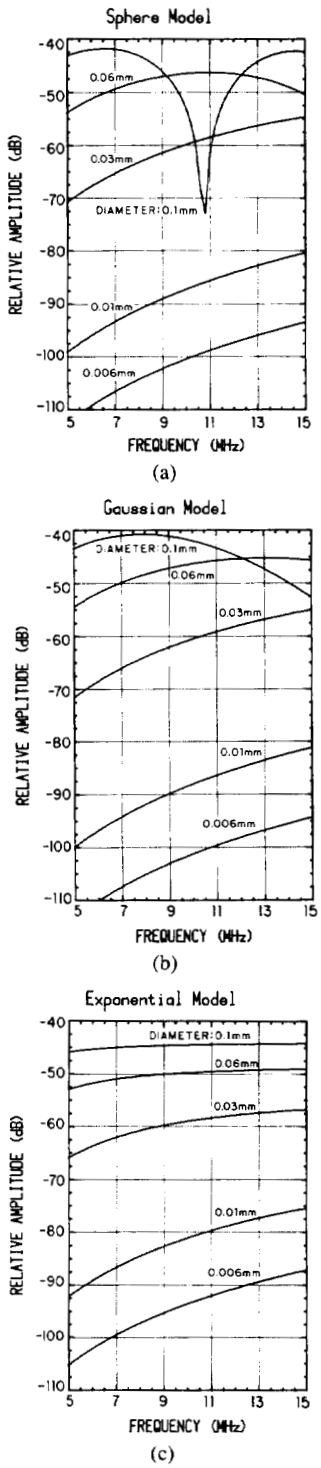

Fig. 5. Theoretical spectra for ocular examinations for different effective scatterer diameters. (a) Sphere model. (b) Gaussian model. (c) Exponential model.

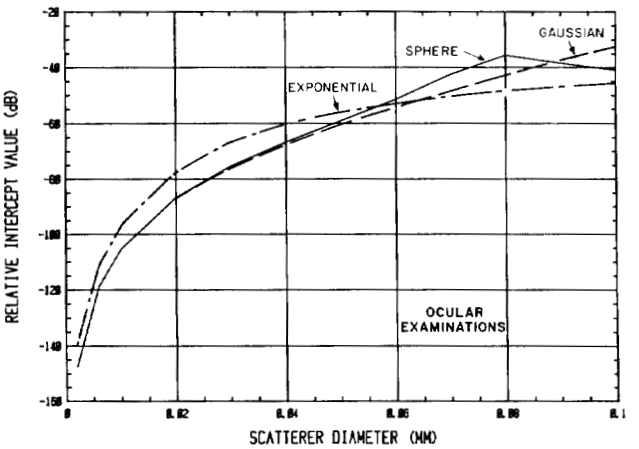

Fig. 6. Spectral intercept values (extrapolated to 0 MHz) obtained by linear regression analysis of computed spectra for different scatterer models with conditions simulating ocular examinations.

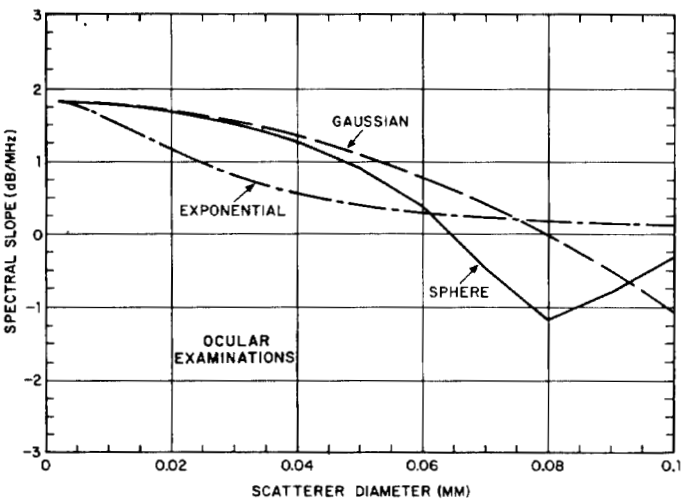

Fig. 7. Spectral slope values obtained by linear regression analysis of computed spectra for different scatterer models with conditions simulating ocular examinations.

In general, the spectral shapes in Fig. 5 resemble those seen in clinical ocular data [6], [7]. As with clinical data, a linear regression analysis has been performed for these theoretical spectra, and the computed values of spectral intercepts and slopes are plotted as functions of scatterer diameter in Figs. 6 and 7. These plots pertain to $CQ^2 = 1$; other values of C and Q increase the intercept value by $10 \log CQ^2$ but do not alter the slope value. (This follows from the fact that K influences spectral amplitude but not spectral shape.)

Figs. 6 and 7 demonstrate that intercept and slope values depend strongly upon scatterer diameter for all analyzed autocorrelation functions. Spectral slope decreases as spectral intercept increases for the range of diameters under consideration. The results for the Gaussian and spherical models are very similar except for diameters near 0.08 mm where spherical resonant phenomena occur. The exponential model exhibits slopes that asymptotically approach zero for large diameters.

Fig. 8 plots these results in a more useful format for comparison with data-base information. Here the spectral intercept is plotted as a function of spectral slope using the results shown in Figs. 6 and 7. As expected from the preceding discussion, the spherical and Gaussian models exhibit the closest agreement. For comparison, the linear fit to our ocular-tumor data base [7] is also shown on this graph; this is the center line through a scatter diagram of tumor data points which are confined to a region of about

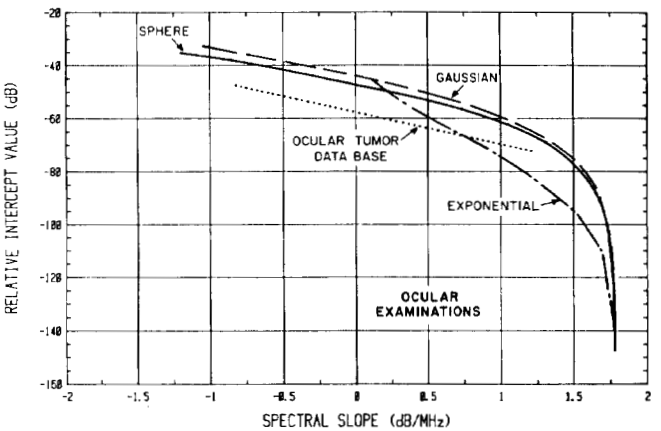

Fig. 8. Spectral intercept values versus spectral slope values computed for different scatterer models with conditions simulating ocular examinations. Linear regression fit to ocular-tumor data base is also shown.

± 5 dB about the line. This data-base line is approximately parallel to the results for the spherical and Gaussian models and is offset by about -10 dB. The offset corresponds to a value of CQ^2 of 10^{-1} mm^{-3}, and when this value is used, the data and theoretical results fit to within a few dB. This value of CQ^2 mentioned earlier would correspond, for example, to a concentration of 100 scatterers/mm^3 and an acoustic impedance differential of three percent. According to the sphere model, the range of scatterer sizes corresponding to the data-base line is approximately 0.03–0.09 mm.

The fact that the clinical data base agrees with theoretical results for a constant value of CQ^2 implies that scatterer size is the most important factor in determining the ranges of spectral intercept and slope values in ocular tumors. However, variations in scatterer concentration or acoustic impedance may be responsible for the variations about the linear data-base fit shown in Fig. 8. For a given slope value these amount to about ± 5 dB. Such departures from the linear fit are diagnostically important and have played a key role in distinguishing among otherwise ambiguous situations.

Since the agreement between the data base and the spherical model is so close, we have employed this model to estimate scatterer size by analyzing measured spectral slopes using the results shown in Fig. 7. In addition, ongoing acoustic microscopy studies are helping to clarify the most appropriate autocorrelation function for various types of tissue.

Fig. 8 reveals an important result regarding the exponential model which predicts that large-diameter scatterers should produce spectra with zero slope values. The ocular data base shows that negative slopes can be produced by ocular tumors (metastatic carcinomas and hemangiomas) that are too small for attenuation to become significant. Likewise, recent results with test targets, consisting of polystyrene particles suspended in a gel block, reveal that negative slopes can be produced by large-diameter scatterers. These clinical and experimental data indicate that the spherical and Gaussian models, which predict negative slopes for these large diameters, are more appropriate for tissue analysis than the exponential model. Size estimates based on the sphere and Gaussian model are also very close as seen in Fig. 7.

B. Liver Scattering

Under the assumptions described earlier, scattering from liver elements is treated following the same approaches already described but using parameters appropriate for abdominal examinations: specifically,

$$a = 5 \qquad R = 60 \qquad 2 \text{ MHz} \le f \le 4 \text{ MHz}.$$

In addition, we consider scatterer diameters that are smaller than 0.8 mm, so we may assume R_D and R_G are constants as described in the preceding section. The effects of intervening attenuation are not included so that the dependence of spectra on primary scatterer features can be evaluated; attenuation effects are discussed subsequently.

Spectra for each of the three autocorrelation models are computed by substituting the foregoing parameters into (10) and setting CQ^2 equal to unity. Individual spectra for different scatterer sizes are shown in Fig. 9. Scatterers smaller than about 0.06 mm produce spectra that are proportional to f^4 as expected for Rayleigh scattering conditions. Increasing the scatterer diameter results in increasing spectral amplitude values and decreasing spectral slope values. At sizes near 0.3 mm the slopes are approximately zero; for large sizes the spherical model exhibits scalloped spectra.

Linear regression parameters for these spectra were computed, and the resultant spectral intercept and slope values are shown in Figs. 10 and 11 for each of the scattering models. Fig. 12 shows the corresponding plots of spectral intercept as a function of spectral slope. As in the ocular case, the spherical and Gaussian models exhibit close agreement, while the exponential model has spectral slopes that asymptotically approach zero for large diameters.

The preceding results do not account for attenuation in intervening tissues. The attenuation multiplies $\hat{S}$ by exp $(-4\alpha d f^n)$ where α is the effective amplitude attenuation coefficient, d is the depth of intervening tissue, and n is usually assumed to be unity, although several investigators have reported values larger than one [14], [15]. Assuming n is unity, spectral measurements expressed in dB exhibit a 0-MHz intercept that is unaffected by this attenuation factor and a slope that is lowered by $-40\alpha d \log e$. In terms of Figs. 10 and 11 the indicated intercept values are not affected, but the slope values are altered in the presence of such intervening attenuation.

Even with attenuation, the preceding results are useful in interpreting clinical data and evaluating the importance of tissue features in influencing spectral results. Under *in-vitro* conditions, liver samples have been found to produce backscattering proportional to approximately f^2 [2]; over the 2–4 MHz band, this corresponds to a slope of about 3 dB/MHz which would be produced by a scatterer

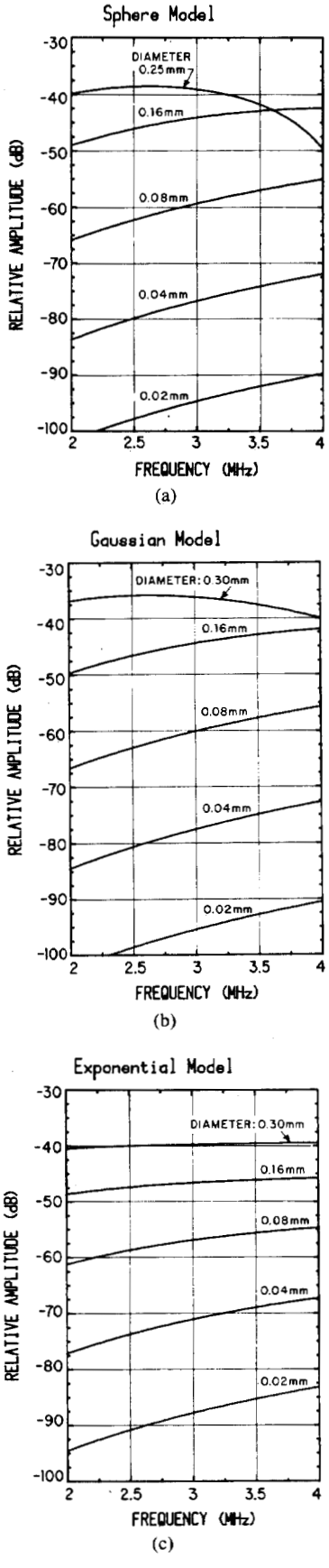

Fig. 9. Theoretical spectra for liver examinations for different effective scatterer diameters. (a) Sphere model. (b) Gaussian model. (c) Exponential model.

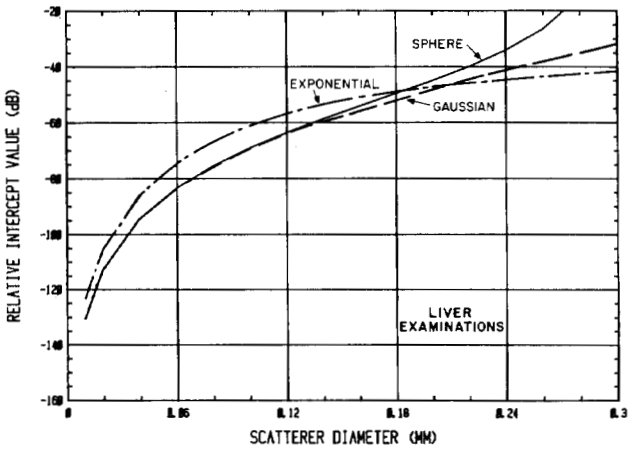

Fig. 10. Spectral intercept values (extrapolated to 0 MHz) obtained by linear regression analysis of computed spectra for different scatterer models with conditions simulating liver examinations.

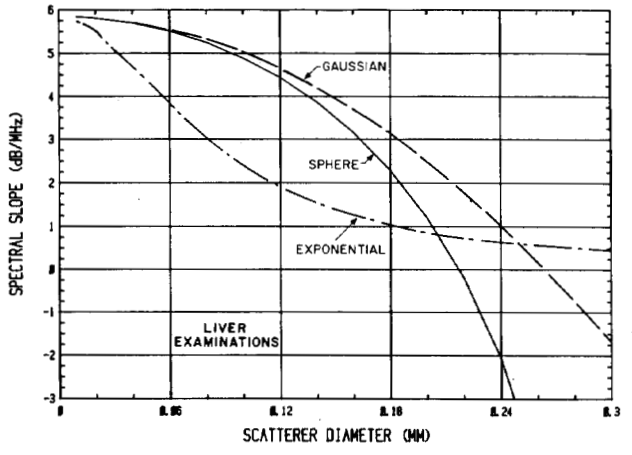

Fig. 11. Spectral slope values obtained by linear regression analysis of computed spectra for different scatterer models with conditions simulating liver examinations.

whose size is approximately 0.18 mm (see Fig. 11). Although this slope value would be altered by attenuation in clinical situations, we can evaluate changes that would be produced by local size inhomogeneities. For example, if the effective scatterer diameter changes by 50 percent from the aforementioned value in one spatial region, Fig. 11 indicates that the slope will change by about 2 dB/MHz. In addition, Fig. 10 indicates that the intercept value (for the same CQ^2) will change by more than 10 dB. These very large alterations indicate the key role played by scatterer size in determining spectral parameters. In contrast, a 10-dB intercept change would require that Q be changed by a factor of 3 or that the concentration be altered by a factor of 10; neither of these changes would alter the spectral slope. Thus the analytic results indicate that spatial variations in scatterer size will produce correlated perturbations in spectral intercept and slope while variations of the same magnitude in either scatterer concentration or impedance will produce smaller perturbations in intercept values and will not affect slope values.

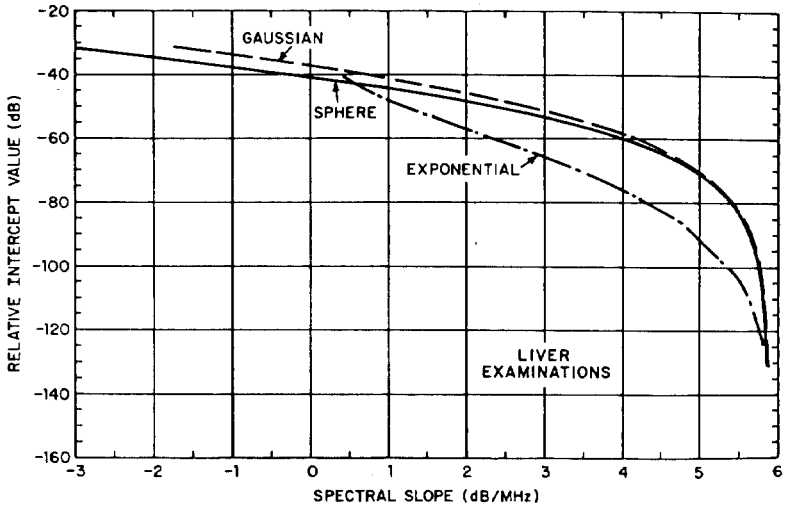

Fig. 12. Spectral intercept values versus spectral slope values computed for different scatterer models with conditions simulating liver examinations.

V. Discussion

The analytical models described here have proven useful in improving our understanding of how tissue features are related to measured ultrasonic characteristics. The results show that effective scatterer size is a predominant factor in determining the slope and intercept values of ultrasonic spectra. The acoustic impedance and concentration of the scatterers influence the spectral intercept only, and relatively large changes in these factors are required to produce intercept changes similar to those produced by modest changes in scatterer size. The relative importance of these tissue features for small scatterers may be examined by letting $k\rho$ approach zero in (10), which describes $\hat{S}$ for each scattering model. Under this condition, spectral amplitude and, therefore, spectral intercept are proportional to the mth power of the scatterer radius where m is 6, 6, and 4 for the spherical, Gaussian, and exponential models, respectively. This high degree of dependence is in sharp contrast to the amplitude's dependence on the second power of differential acoustic impedance and the first power of scatterer concentration.

In ophthalmology the analytical results are of direct use in interpreting clinical spectra in terms of morphological features because intervening attenuation is not significant with properly chosen beam placement. Comparison with our ocular-tumor data base shows that the correlation we have observed between spectral slope and intercept values is consistent with that expected from variations in effective scatterer size; according to the analytic results, these sizes are generally in the range of 0.03–0.09 mm. Relatively small, but diagnostically important, intercept changes of about ± 5 dB have been observed for a given spectral slope; these are presumably induced by the different acoustic impedances and concentrations of scatterers that exist in different tumors.

We are now using these results to estimate properties of morphological features within ocular tumors. Specifically, observed spectral slopes are used to estimate effective scatterer size using either the sphere- or Gaussian-model results shown in Fig. 7. Next, the influence of this size on intercept values is computed and subtracted from observed intercept values using the results shown in Fig. 6. The residual intercept value is then used to compute values of the parameter CQ^2. This approach is particularly promising since it permits us to present clinical results in terms of physical tissue features rather than in terms of measurement parameters. When the approach is applied to average power spectra, useful bounds can be placed on the average values of each tissue property within the examined tumor. We have also applied this technique to local computations of spectra in contiguous small regions within tumors. The resulting size estimates are then used to generate cross-sectional images in which color depicts the estimated range of scatterer sizes throughout a tumor [10]. Such depictions are helping us understand internal morphological variations and are providing a means for comparing clinical spectral data with histopathology.

In terms of liver examinations the model is providing a fundamental framework for clinical interpretation and for refining our techniques. Here intercept values can be interpreted quantitatively, provided intervening attenuation varies as the first power of frequency, as is often assumed. The slope values cannot be interpreted in an absolute sense because of intervening attenuation. However, changes in slope can be related to changes in scatterer size; an initial review of our liver data base shows that such slope changes are often accompanied by intercept changes with magnitudes close to those predicted by Fig. 11 for diameters near 0.2 mm.

A number of topics involving ocular and liver examinations are now under active study. The question of which model is most appropriate for the tissue's autocorrelation function is being addressed through acoustic microscopy studies. As noted earlier, the sphere and Gaussian models

seem more relevant for tissue analysis than the exponential model, which is inconsistent with the negatively sloped spectra seen in many small ocular tumors and in test objects. The statistics of feature estimation [13], [16] are being reexamined to determine how accurately we can evaluate tissue features based on our spectral techniques. Test targets with different sizes, concentrations, and impedances of constituent scatterers are also being employed to verify details of the model; a report is in preparation describing these results which to date have shown excellent agreement with theoretical results for the sphere and Gaussian models.

Acknowledgment

The authors gratefully acknowledge the contributions and assistance of their colleagues in the Biomedical Engineering Laboratories at Riverside Research Institute. Special acknowledgment is given to Dr. D. J. Coleman, M.D., and Dr. D. L. King, M.D., and their staff members at the Cornell University Medical College and Columbia-Presbyterian Medical Center, respectively. We also wish to thank I. Gilston, J. Gallon, and J. Walls for their diligent assistance in manuscript preparation.

References

[1] R. C. Kuc, "Clinical application of an ultrasound attenuation estimation technique for liver pathology characterization," *IEEE Trans. Biomed. Eng.*, vol. BME-27, pp. 313-319, 1980.

[2] D. Nicholas, "Evaluation of backscattering coefficients for excised human tissues: Results, interpretation and associated measurements," *Ultrasound Med. Biol.*, vol. 8, pp. 17-28, 1982.

[3] R. C. Waag, P. P. K. Lee, H. W. Persson, E. A. Schenk, and R. Gramiak, "Frequency dependent angle scattering of ultrasound by liver," *J. Acoust. Soc. Amer.*, vol. 72, pp. 343-352, 1982.

[4] O'Donnell, J. W. Mimbs, and J. G. Miller, "The relationship between collagen and ultrasonic attenuation in myocardial tissue," *J. Acoust. Soc. Amer.*, vol. 65, pp. 512-517, 1979.

[5] F. G. Sommer *et al.*, "Spleen structure in Hodgkin disease: Ultrasonic characterization," *Radiology*, vol. 153, pp. 219-222, 1984.

[6] D. J. Coleman and F. L. Lizzi, "Computerized ultrasonic tissue characterization of ocular tumors," *Amer. J. Ophthalmology*, vol. 96, pp. 165-175, 1983.

[7] D. J. Coleman *et al.*, "A model for acoustic characterization of intraocular tumors," *Investigative Ophthalmology Visual Sci.*, vol. 26, pp. 545-550, 1985.

[8] D. J. Coleman *et al.*, "Regression of uveal malignant melanomas following cobalt-60 plaque: Correlates between acoustic spectrum analysis and tumor regression," *Retina*, vol. 5, pp. 73-78, 1985.

[9] D. L. King *et al.*, "Focal and diffuse liver disease studied by quantitative microstructure sonography," *Radiology*, vol. 155, pp. 457-462, 1985.

[10] E. J. Feleppa, F. L. Lizzi, D. J. Coleman, and M. Yaremko, "Diagnostic spectrum analysis in ophthalmology: A physical perspective," *Ultrasound Med. Biol.*, vol. 12, no. 8, pp. 623-631, 1986.

[11] F. L. Lizzi and E. J. Feleppa, "Computer analysis and display modes for diagnostic ultrasound," in *Proc. 4th Ann. Conf. IEEE Engineering in Medicine and Biology Soc.*, A. R. Potvin and J. H. Potvin, Eds. New York: IEEE, 1982, pp. 544-550.

[12] F. L. Lizzi, M. Greenebaum, E. J. Feleppa, M. Elbaum, and D. J. Coleman, "Theoretical framework for spectrum analysis in ultrasonic tissue characterization," *J. Acous. Soc. Amer.*, vol. 73, pp. 1366-1373, 1983.

[13] F. L. Lizzi, M. Laviola, and D. J. Coleman, "Tissue signature characterization utilizing frequency domain analysis," in *Proc. IEEE Ultrasonics Symp.*, 1976. New York: IEEE, pp. 714-719.

[14] K. J. Parker, R. M. Lerner, and R. C. Waag, "Attenuation of ultrasound: Magnitude and frequency dependence for tissue characterization," *Radiology*, vol. 153, pp. 785-788, 1984.

[15] P. A. Naryana and J. Ophir, "On the validity of the linear approximation in the parametric measurement of attenuation in tissues," *Ultrasound Med. Biol.*, vol. 9, pp. 357-361, 1983.

[16] F. Lizzi, E. Feleppa, M. Rorke, M. Yaremko, and J. Hui, "In-vivo estimation of attenuation and images of related parameters," in *Proc. 4th European Communities Workshop*, Ferrara, J. Thijssen, Ed. Nijmegen, The Netherlands: Univ. Nijmegen, 1986, pp. 45-56.

Frederic L. Lizzi (S'62-M'71) was born in Brooklyn, NY, in 1942. He received the B.E.E. degree from Manhattan College, Bronx, NY, in 1963 and the M.S. and Ph.D. degrees from Columbia University, New York, NY, in 1965 and 1971, respectively.

In 1967 he joined the research staff of the Electronics Research Laboratories of Columbia University (currently Riverside Research Institute) where he worked on therapeutic and diagnostic ultrasound. He is currently Research Director for Biomedical Engineering at Riverside Research Institute, New York, NY. He serves as principal investigator for a number of research programs, supported by the National Institutes of Health, dealing with ultrasonic imaging, tissue characterization, and therapeutic ultrasound. He was a Research Associate at the College of Physicians and Surgeons of Columbia University and is an Adjunct Professor at Cornell University Medical College.

Dr. Lizzi is a fellow of the American Institute of Ultrasonics and Medicine (AIUM), and a member of the SIDUO, and the American Association for the Advancement of Science. He is a member of the WFUMB Safety Committee, coeditor of a recent special Bioeffects Edition of the IEEE TRANSACTIONS ON SONICS AND ULTRASONICS, and a member of Advisory Editorial Board of Ultrasound in Medicine and Biology. He is a member of the Board of Governors of the AIUM and is Chair of the AIUM Bioeffects Committee.

Michael Ostromogilsky was born in Kiev, USSR. He received the B.S. and M.S. degrees in electrical engineering from Columbia University, New York, NY, in 1980 and 1982, respectively.

He is currently a Member of the Research Staff at Riverside Research Institute, New York, NY. His major interests are the theoretical bases of ultrasonic scattering and wave propagation.

Mr. Ostromogilsky is a member of Sigma Pi Sigma.

Ernest J. Feleppa (M'82) received the B.A. degree in physics from Cornell University, Ithaca, NY, in 1961 and the Ph.D. degree in biophysics from Columbia University, New York, NY, in 1968. His doctoral dissertation concerned applications of holography and optical spatial filtering to biology and medicine. His postdoctoral studies investigated the physiological and genetic bases of development.

Since joining the staff at Riverside Research Institute, New York, NY, he has led projects involving ecological and environmental studies, management systems design and implementation and biomedical engineering. He has been a member of the Biomedical Engineering Laboratory staff since 1976 where he participated in the development of ultrasonic tissue characterization systems, techniques, software, and theory and in studies of the biological effects of ultrasound.

Mary C. Rorke was born in Brooklyn, NY. She received the B.S. degree in electrical engineering with a concentration in bioengineering in 1981, and the M.S. degree in electrical engineering in 1985 from the Polytechnic Institute of New York.

She has been a Member of the Research Staff at Riverside Research Institute, New York, NY, since June 1981. Her major areas of interest are signal and image processing.

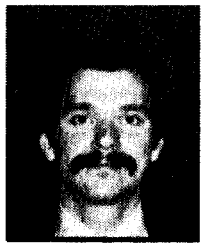

Mykola Yaremko (S'76–M'78–S'82–M'86) was born in New York, NY. He received the B.E. degree in electrical engineering from Cooper Union, New York, NY, in 1978 and the M.S.E.E. degree from Stevens Institute of Technology, Hoboken, NJ, in 1982.

He has been a Member of the Research Staff at Riverside Research Institute, New York, NY, since 1978. His interests are in diagnostic ultrasound, image processing, and personal computers.